Effects of a Discontinuous Surface Stress on a Model of Coastal Upwelling

S. NARIMOUSA AND T. MAXWORTHY*

Department of Mechanical Engineering, University of Southern California, Los Angeles, CA 90089

(Manuscript received 13 September 1985, in final form 24 June 1986)

ABSTRACT

We report on laboratory model experiments in which coastal upwelling was created by a radially discontinuous surface stress in the presence of bottom topography in the form of a ridge. An anticyclonic torque was thus applied to the surface of the fluid at the location of the stress discontinuity which, in turn, generated large, offshore cyclonic and anticyclonic eddies in the stress-free region. When the upwelled front interacted with this offshore eddy field, dense, upwelled water was transported far offshore as jetlike flows. The strong interaction between the stress discontinuity "front" and the upwelled front at the ridge resulted in an upwelling maximum and a downstream jet at the ridge that were weaker than those reported previously by Narimousa and Maxworthy. One observation of interest was that a large number of flow-marking particles accumulated in the region where the ridge intersected the stress discontinuity.

1. Introduction

The coastal upwelling phenomenon has become one of the most interesting and actively pursued aspects of geophysical fluid flows and oceanography. The most active recorded coastal upwelling occurs adjacent to the west coasts of North America (Mooers et al., 1976; Halpern, 1976), South America (Brink et al., 1980) and West Africa (Halpern, 1977). In general, an up-welling favorable, equatorward, alongshore wind stress causes the warm surface water to drift away from the coast and allows nutrient-rich, cold, subsurface water to upwell and appear at the surface near the coast in a narrow band of width λ. The two masses of cold and warm water are separated by a sharp front. This front continues to migrate farther outward, allowing more cold deep water to upwell so that λ increases until, eventually, the front becomes stationary, i.e., $\lambda = \lambda_s$ (see Narimousa and Maxworthy, 1985, hereafter NM1). Some time before this, i.e., when $\lambda = \lambda_i < \lambda_s$, the density front becomes unstable to baroclinic waves (see also Saunders, 1973; Griffiths and Linden, 1981). These features, which are a result of the effects of the earth rotation acting together with the wind stress on the upwelling front, have many interesting properties influencing the dynamics of the coastal upwelling circulation. For example, the frontal instabilities can grow to such a large amplitude that cyclonic waves pinch off from the front (NM1). These cyclones then carry the cold, bottom water farther offshore to produce isolated cold ring eddies in the surrounding warm water

(Rienecker et al., 1985). Furthermore, satellite images (Flament et al., 1985; Breaker and Mooers, 1985) and field measurements (Mooers and Robinson, 1984) indicate the presence of cold jets originating from the front and meandering offshore through the warmer water. It is believed (see Mooers and Robinson; NM1) that it is the interaction of cyclones and anticyclones near the front that produce these observed cold filaments, a process discussed in detail in Narimousa and Maxworthy (1986a, hereafter NM2).

Observations of satellite infrared (IR) images reveal the presence of isolated, warm, anticyclonic, offshore rings (Simpson et al., 1984; Bernstein et al., 1977; Huyer et al., 1984). These warm rings, unlike the cold rings, do not appear to be a result of a "pinch-off" process from the upwelled front and may be caused by an entirely different mechanism, which will be discussed later in this paper. According to Hickey (1979) and Nelson (1977), there is a positive curl in the southward component of the summertime mean wind stress off of the west coast of the United States. It is the focus of this study to produce an offshore curl (see §2) and examine its effects on the upwelling front upstream and downstream of a bottom topographic feature. As will be demonstrated in sections 3 and 5, this wind-stress curl plays an important role in generating large-scale offshore eddies; in the experiments of NM1, where such a curl was absent, no offshore eddies were observed. In sections 3 and 5 we discuss the interaction between these offshore eddies and the upwelled front, and the consequent offshore transport of upwelled water. Due to the important role played by the offshore eddies in transporting upwelled water offshore, we study here their behavior as the value of a control parameter $\theta_* = g'h_0/u_* f\lambda_s$ varies. Note that θ_*

---

* Also affiliated with the Department of Aerospace Engineering, University of Southern California, and Earth and Space Sciences Division, Jet Propulsion Laboratory.

$= \mathrm{Ri}_*^{1/2}\theta$, where $\mathrm{Ri}_* = (g'h_0)/u_*^2$ is the Richardson number and $\theta = (g'h_0)^{1/2}/f\lambda_s$ is the dimensionless Rossby deformation radius. Here $g' = g\delta\rho$ is the reduced gravity, $\delta\rho$ the density difference between top and bottom layers, h_0 the depth of the top layer, u_* the friction velocity applied to the top surface, f the Coriolis parameter, and λ_s the width of the stationary region of dense upwelled water. As in NM1, we also study the behavior of the downstream standing waves as the values of θ_* vary.

2. The experiment

We used the same apparatus as in NM1 to study coastal upwelling caused by a discontinuous surface stress and the presence of bottom topography. For a detailed discussion of the experimental apparatus and procedure the reader is referred to NM1. Only a brief discussion will be given here.

Two layers of saltwater of slightly different densities were brought to solid-body counterclockwise rotation inside a cylindrical tank (90 cm in diameter and 22 cm in depth) having a conical bottom with a radial topographic ridge (Fig. 1). The ridge had a maximum width of 7.6 cm at the wall, gradually reducing to zero at the center of the tank (Fig. 3). The maximum height of the ridge was 3.2 cm at the wall, and it was cut so as to extend 3.8 cm outward to produce a capelike feature. Beyond this, the height of the ridge gradually reduces to zero at the center of the tank. The surface of the top fluid was in contact with a circular, smooth disc, so that as the disc rotated differentially a stress was applied to the top surface of the less dense water in order to model the wind stress at the air–sea interface. In this study the disc was rotated in a clockwise direction, i.e., opposite to the basic rotation of the ap-

paratus. The tank was only partially filled so that the surface of the top layer was only in contact with the outer D cm of the disc (see Figs. 1 and 5). Thus, the stress applied to the top surface was discontinuous at D, and a strong negative surface-stress curl occurred at this location. This experimental arrangement produced an alongshore horizontal velocity profile in the top layer similar to that calculated by Ikeda et al. (1984), as shown in Fig. 2. In both cases the offshore horizontal velocity rises rapidly to a peak and then drops back to zero more gradually. The nearshore velocity gradient is much greater in the experiments, but this is of little concern to us since we are primarily interested in examining the effect of the gradually decreasing horizontal velocity farther offshore. In this region the experimental velocity gradients are indeed comparable to those calculated by Ikeda et al. (1984).

The applied stress caused the top layer to drift outward (toward the center of the tank) and the interface (front) between the two fluids to rise near the wall. As this process continued, the front intersected the disc surface and then migrated away from the wall, allowing the bottom fluid to appear at the surface around the outer edge of the tank. This frontal movement was observed by placing small, neutrally buoyant particles in the front and recording their motion by streak photography. The direction of motion of these particles was found by firing an electronic flash at the beginning of the time exposure.

According to NM1, the distance of the stationary upwelled surface front from the wall of the tank, λ_s, can be estimated from

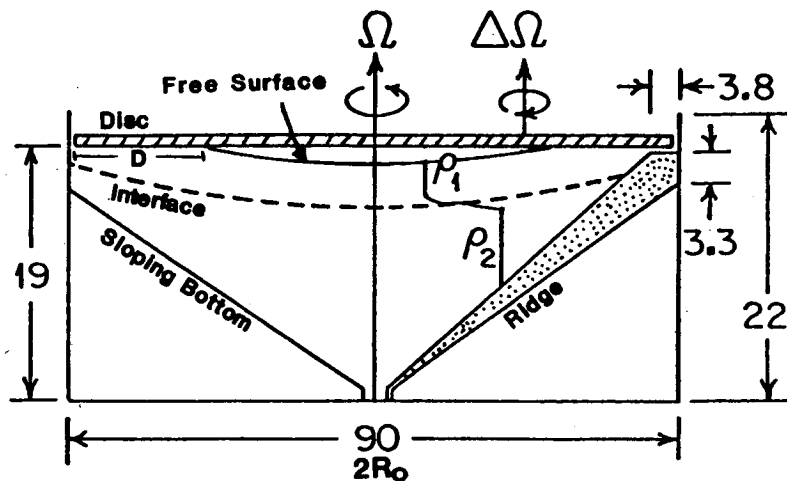$$\frac{\lambda_s}{R_0} = 1 - 0.73\Theta_*^{0.25}, \qquad (1)$$

FIG. 1. Cross-sectional side view of the experimental tank, showing the ridge and the position of the stress discontinuity. Lengths in centimeters. The conical bottom has a slope of about 0.27.
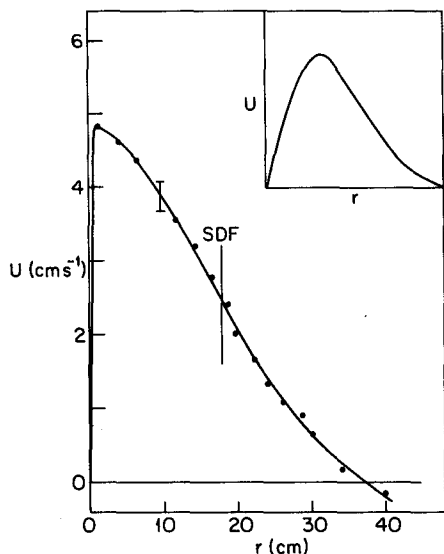
FIG. 2. Typical variations in mean alongshore horizontal velocity U as a function of the offshore distance r. Position of the stress discontinuity front is denoted by SDF. A typical velocity profile with an arbitrary scale from Ikeda et al. (1984) is shown in the upper right corner.

where

$$\theta_* = \frac{g'h_0}{f\Delta\Omega R_0{}^2},$$

$\Delta\Omega$ is the angular velocity of the top disc and R_0 is the radius of the tank. We note that (1) was obtained from a geostrophic balance between the radial pressure gradient caused by front deformation and the radial Coriolis forces; for details see NM1 (also Linden and Van Heijst, 1984). In the present study we discuss two types of experiments. In the first type, $D > \lambda_s$ and only a weak interaction occurred between the upwelled front and the surface stress curl. In the other experiments, $D \leqslant \lambda_s$ and the upwelled front interacted strongly with the surface stress curl.

To reveal the structure of the offshore jets, in some of our experiments, a white, liquid Titanium dye was introduced at the wall near the surface of the upwelled water. The density of the dye was lower than that of both layers and so remained near the surface to reveal the flow activities within the upwelled water near the surface. When this dye was released near the wall it was advected downstream by the mean flow, while at the same time it drifted offshore due to the Ekman layer flow. As a result, when the dye eventually reached the front at some distance downstream from its origin, it revealed the wave activity at the front and was also transported offshore when the upwelled front interacted with the offshore eddies; for details see section 6.

For the present experiments, the basic parameters take the following values: initial depth of the top layer is $2 \leqslant h_0 \leqslant 2.4$ cm; density difference ($\delta\rho_0 = \rho_2 - \rho_1$) between the two layers $0.022 \leqslant \delta\rho_0 \leqslant 0.05$ g cm^{-3};

reduced gravity between the two layers $21.6 \leqslant g' \leqslant 49$ cm s^{-2} (where $g' = g\delta\rho_0$, and $g = 981$ cm s^{-2} is the acceleration of gravity); the Coriolis parameter $2.7 \leqslant f \leqslant 4.65$ rad s^{-1}; the friction velocity $0.24 \leqslant u_* \leqslant 0.42$ cm s^{-1}; the stationary width of the upwelled layer $6.7 \leqslant \lambda_s \leqslant 18.4$ cm; and the control parameter $1.8 \leqslant \theta_* \leqslant 17.3$.

3. Description of the flow field

Here we are concerned with the existence of two discontinuities, one at the density interface (upwelling front) and the other at the location beyond which the top fluid was stress free (SDF, see Fig. 3). Observations from a series of experiments at small values of θ_*, but allowing $\lambda_s < D$, have indicated that the characteristics of the flow upstream, over and downstream of the ridge were very similar to those reported by NM1. Baroclinic waves appeared at the upwelled front upstream of the ridge. Also, a high-speed jetlike flow extended a considerable distance downstream of the ridge in the form of standing waves. Here the presence of the stress curl created offshore eddies like (A) at the location of the stress discontinuity, upstream of the ridge, as seen in the bottom left corner of Fig. 3. Since such features were absent in the experiments of (NM1), we believe that the stress discontinuity was the source for the generation of these eddies. It is characteristic of these eddies that they move "seaward," i.e., toward the tank center and in the direction of the applied stress (as seen in Fig. 3). This figure also shows that (A) existed for more than 20 rotation periods, when it was still visible in the form of a permanent eddy drifting very slowly in the direction of the applied stress. Often an anticyclonic eddy (B), with a shorter life, was also observed downstream of the ridge, near the crest of the first large standing wave and close to the stress discontinuity (see Fig. 3).

Later, when the density front had evolved long enough to be closer to the SDF, so that frontal waves interacted weakly with the stress discontinuity, a different phenomenon occurred. As seen in Fig. 3c, the size of the upstream frontal waves increased to almost twice the value found initially and as given in NM1. At higher values of θ_* and still with $\lambda_s < D$, the dynamics of the flow was similar to that described above for small θ_*. However, since θ_* was larger, the sizes of the frontal waves and offshore eddies and the distance of the standing wave from the ridge were larger also (see Fig. 4).

In the experiments for which $\lambda_s \geqslant D$, the behavior of the density front upstream of the ridge, during front migration and before any interaction with the SDF, was similar to that discussed above, while the dynamics of the flow at the ridge was sometimes different and more complicated. Figure 5 shows some of these complex flow patterns at the ridge, which should be compared with the photographs of NM1 and Fig. 3. The interaction of the SDF with the high-speed jet at the
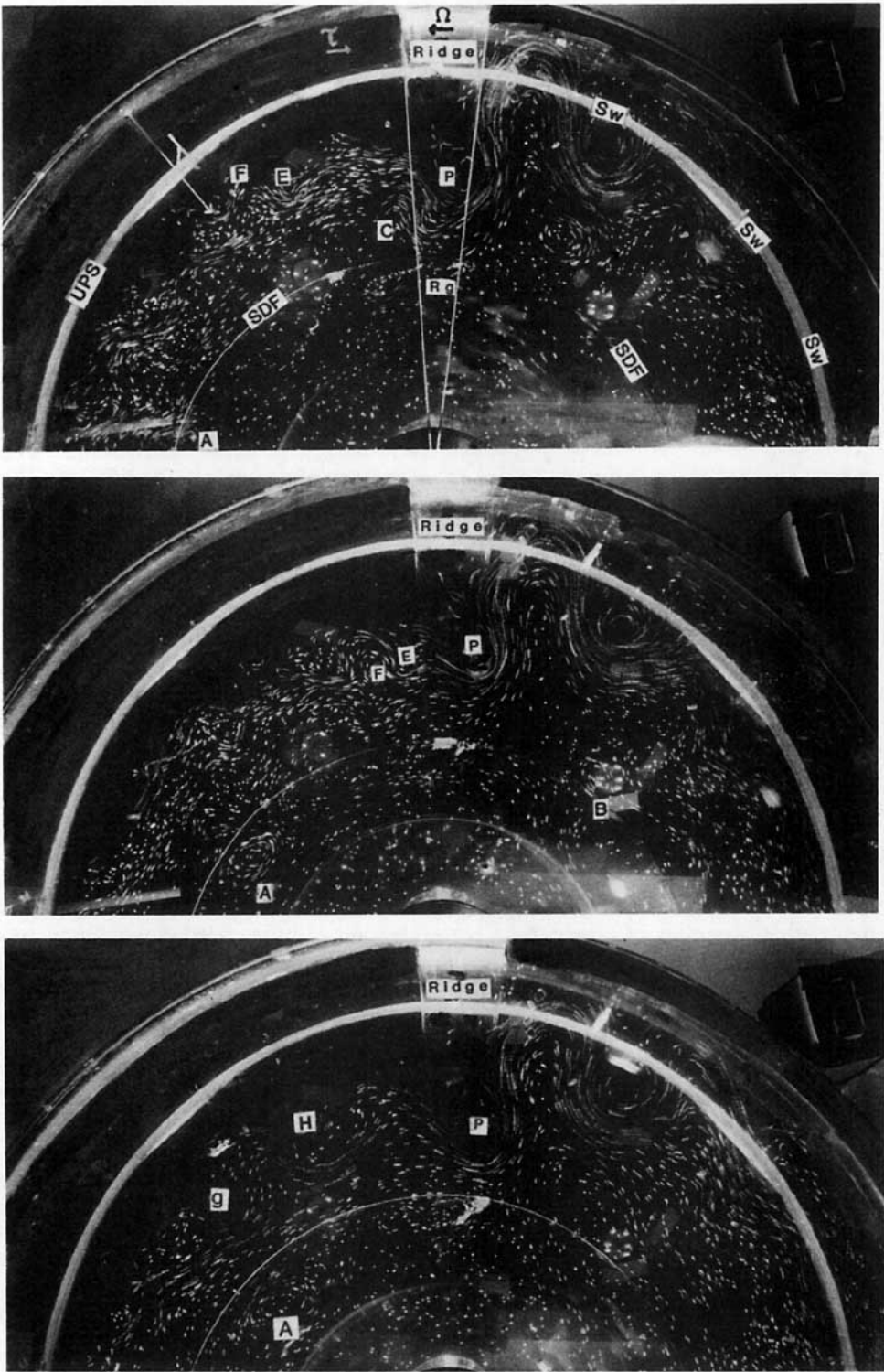
FIG. 3. A set of streak photographs for parameter values; rotation rate $f = 2\Omega = 4$ s^{-1}; differential rotation of the disc $\Delta\Omega = 0.125$ s^{-1}; initial depth of the less dense top layer $h_0 = 2.2$ cm; the density difference between the two layers $\delta\rho_0 = 0.021$ g cm^{-3}; the disc friction velocity $u_* \approx 0.26$ cm s^{-1}; $\theta_* = g'h_0/u_* f \lambda_s \approx 2.7$; $\lambda_s \approx 15.7$ cm; and $D = 22.5$ cm. In these photographs the region around the outer edge of the tank, with no particles, indicates the width of the bottom upwelled flow (λ) as shown in (a) (upper panel). There is an upwelling maximum, in the form of a plume (p), which always occurs at the ridge (Rg). The downstream high-speed jet forms standing waves (sw) as shown in (a). Photograph (a) was taken $61T$ after the start of the experiment (where T is the rotation period), at which stage $\lambda \approx 11$ cm. The generation of the offshore anticyclonic eddy (A) at the stress discontinuity front upstream of the ridge (UPS) and (B) downstream near the crest of the first standing wave is clear. Also notice the approaching baroclinic anticyclonic eddies E (cyclonic) and F (anticyclonic) upstream of the ridge. Photograph (b) (middle panel), taken after $67T$, shows
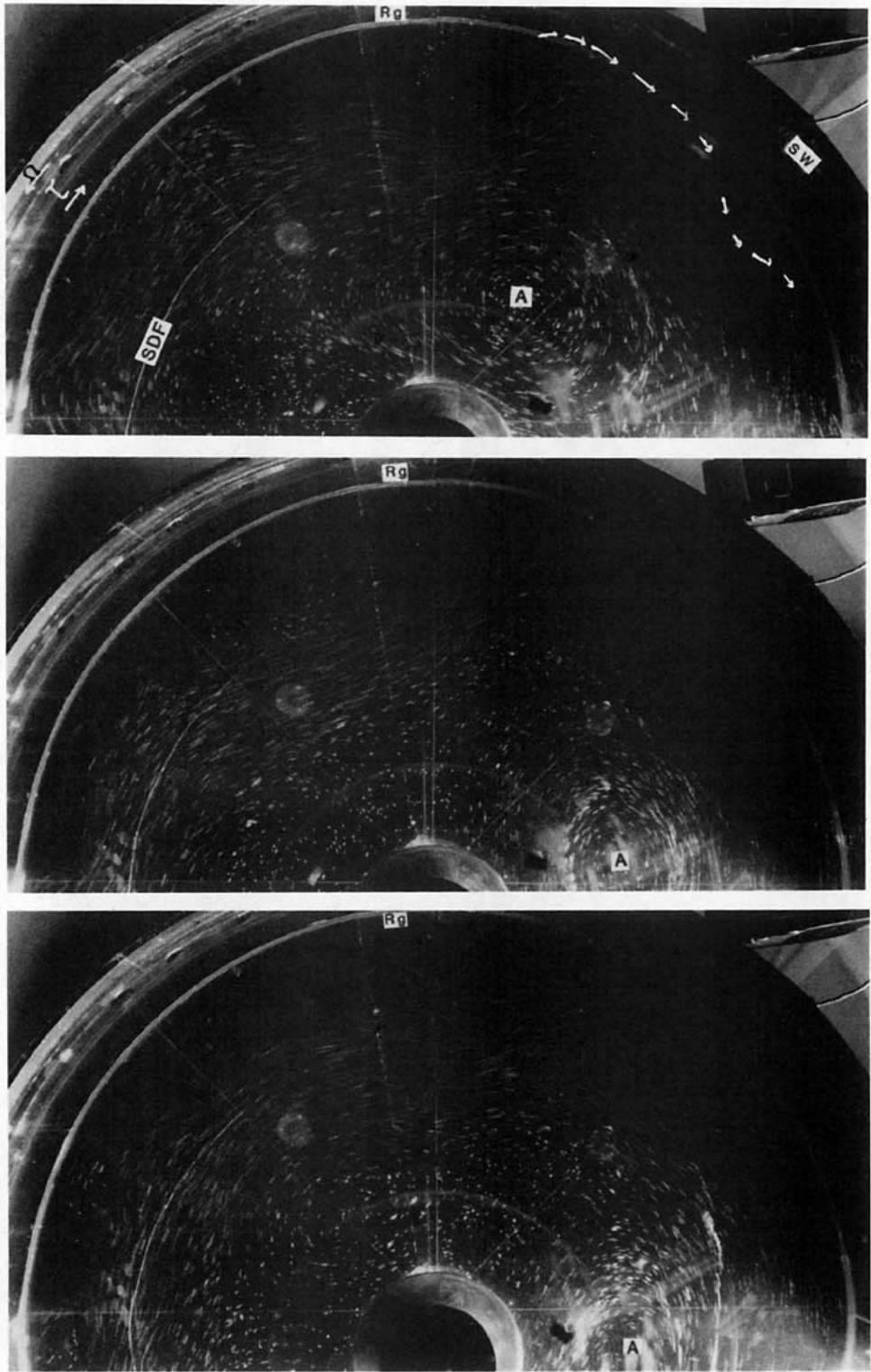
FIG. 4. A set of streak photographs, with a 0.5 s time exposure, from an experiment with $f = 2.7 \text{ s}^{-1}$; $\Delta\Omega = 0.143 \text{ s}^{-1}$; $h_0 = 2.4$ cm; $g' = 39 \text{ cm s}^{-2}$; $u_* = 0.38 \text{ cm s}^{-1}$; $\lambda_s \approx 7.5$ cm; $D = 17.6$ cm; and $\theta_* \approx 12.3$. Photograph (a) (upper panel), taken after $73T$, shows an anticyclone (A), which has almost passed the ridge. Photographs (b) (middle panel) and (c) (lower panel), taken after $95T$ and $104T$, show that (A) has drifted downstream.

that (A) has drifted into the stress-free region, while (B) has not and is about to lose its identity; E and F are now very close to the ridge. Photograph (c) (lower panel), taken after $81T$, shows eddy (A), which has slowed considerably to become a semistationary eddy, while (B), (E) and (F) have vanished. A large increase in the size of the frontal waves (G and H) in comparison with those (E and F) seen in the previous photographs can also be observed.
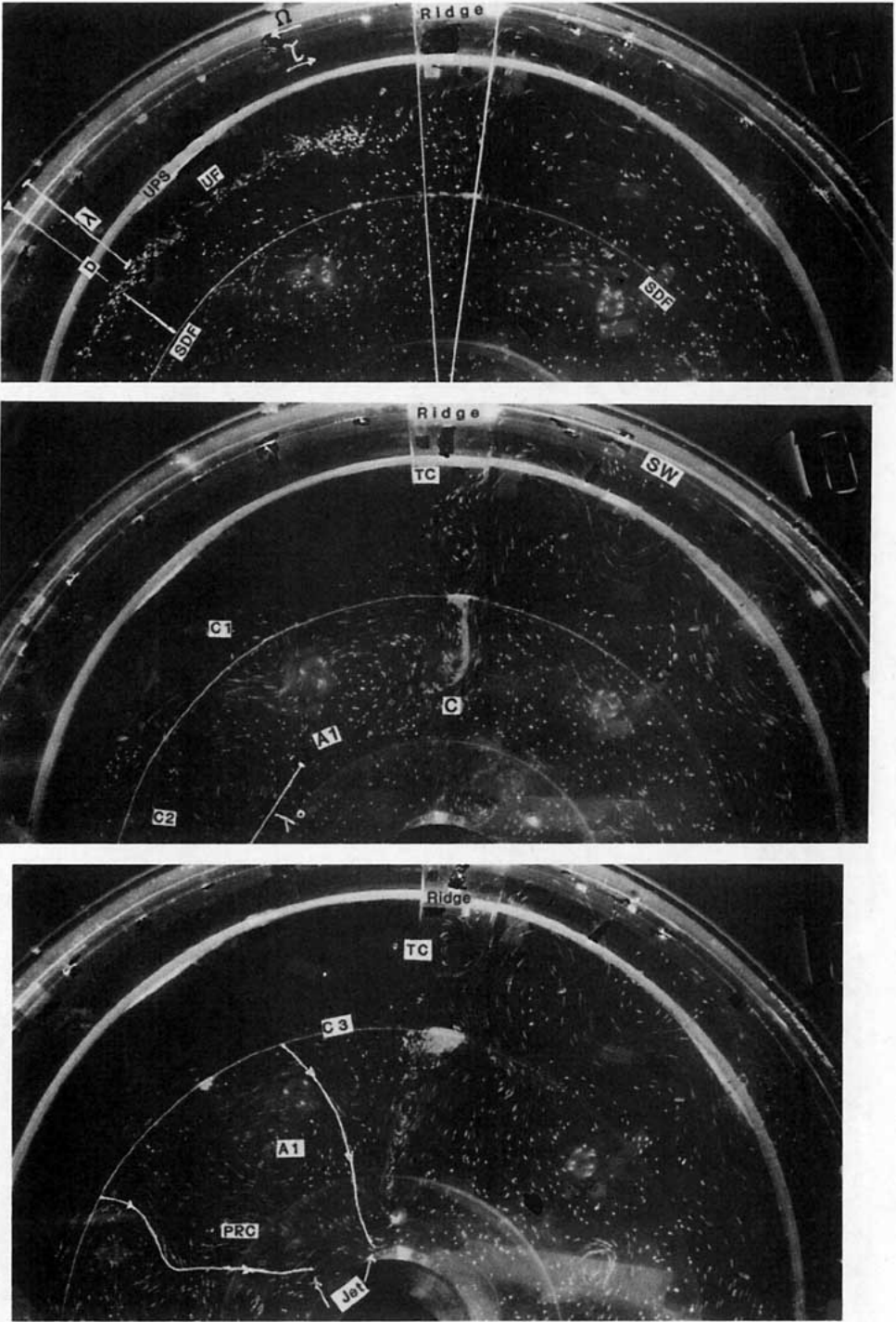
FIG. 5. A set of streak photographs, with 0.5 s time exposure. Parameter values: $\Omega = 2.3$ s^{-1}; $\Delta\Omega = 0.125$ s^{-1}; $h_0 = 2.1$ cm; $\delta\rho_0 = 0.024$ g cm^{-3}; disc friction velocity $u_* \approx 0.24$ cm s^{-1}; $\theta_* = 2.2$; $\lambda_s \approx 17.3$ cm; and $D \approx 17.5$ cm. Photograph (a) (upper panel) was taken after about $13T$ and shows a well-defined upwelled front (UPS) upstream of the ridge. In this photograph, unlike a similar one in NM1 and Fig. 3, the high-speed jet and the upwelling maximum at the ridge are absent, indicating the strong influence of the SDF on the upwelled front at the ridge. Also, notice that the downstream jet (DS) in these photographs is not as intense as that reported by NM1 and in Fig. 3. Photograph (b) (middle panel), taken after $47T$, shows large offshore eddies [A_1 (anticyclonic) adjacent to the ridge and C_2 (cyclonic) upstream of A_1] in the stress-free region. Notice the development of a large cyclone [C_1 at the (SDF)] and also the trapped cyclones (TC) at the ridge. The one in the stress-free region has a number of particles accumulated within it, and the other one is in the applied-stress region. In this photograph the upstream waves have interacted with the (SDF) and lost their energy to the large offshore eddies. In photograph (c) (lower panel), taken at about $100T$, (A_1) has migrated upstream allowing a new cyclone (C_3) to develop adjacent to the ridge, while (C_1) and (C_2) have paired to become (PRC). Notice the presence of the outward meandering jets as a result of the interaction between the counterrotating offshore eddies. Also notice that the head of the (TC) in the stress-free region has propagated offshore and generated small cyclones containing many particles.

ridge also influenced the dynamics of the flow downstream. For example, for the value of $\theta_* \approx 2.2$, based on the observations of NM1, one would expect the photographs of Fig. 5a to show a series of standing waves downstream of the ridge. However, in Fig. 5a, the presence of these standing waves is not apparent (cf. Fig. 3). In Figs. 5b and 5c, such standing waves are generated, but they are different from those seen before, with the first standing wave having a longer wavelength and a smaller amplitude than those of NM1 and Fig. 3.

When the upwelled front upstream of the ridge migrated to the neighborhood of the SDF, the baroclinic waves began to interact with the SDF. The first sign of this interaction is shown in Fig. 5b, where a dramatic change in appearance of the flow field upstream of the ridge is apparent when compared to NM1. Here a number of large, stationary cyclonic and anticyclonic offshore eddies were produced in the stress-free region (see Fig. 5b). In Fig. 5b and 5c the upwelled front has interacted with the SDF. An important feature of the flow upstream of the ridge was the development of a large, semipermanent anticyclonic eddy adjacent to the upstream edge of the ridge, the signature of which became stronger with time (see Fig. 5b and 5c). When fully developed, this anticyclone drifted slowly upstream in a direction opposite to that of the applied stress. This then caused a cyclone to develop in its place. Later, this cyclone reached a size typical of the other large offshore eddies, and it also drifted in the upstream direction to allow yet another new anticyclone to develop adjacent to the ridge. Within the field of offshore eddies there were always a number of counterrotating vortices, each pair of which produced an offshore, meandering jet, as seen in Fig. 5c.

A high-speed, jetlike flow developed at the ridge, in the form of a loop with a weak upwelling flow within it (cf. Maxworthy, 1977). This is shown in Fig. 5b, where the presence of stationary particles indicates the weakness of the upwelling maximum at the ridge. However, as seen in Fig. 5c the head of the high-speed jet sometimes became unstable. As it began to grow in amplitude, its curvature increased and it generated small cyclones (C in Fig. 5).

An interesting and potentially important feature of the flow at the ridge was the existence of a large concentration of particles at the intersection of the downstream edge of the topography and the stress-free region (see Fig. 5b and 5c). Since such a concentration of particles was not observed in NM1, the influence of the SDF on the upwelled front at the ridge is the most likely reason for the concentration of these particles. Such a region of surface convergence may play an important role in the concentration of marine life, waste material and, perhaps, oil slicks in natural flows.

4. Results

Our measurements of events such as the migration rate of the upstream, upwelled front at the surface $u_f/$

u_* (u_f is the radial speed of the front at the surface), the appearance of upstream baroclinic circular waves at the upwelled front when it was a distance $\lambda_i < \lambda_s$ away from the wall of the tank, the average diameter of the circular baroclinic waves λ_w, and their drift velocity u_w in the direction of the applied stress, for the case in which the upwelled front was not influenced by SDF, gave the same results as those already given in NM1 and NM2; hence, we do not repeat them here. On the other hand, when the upstream, upwelled front interacted with SDF, the situation was different from that in NM1 (see §3), since the migration of the upwelled front at the surface was forced to stop and the frontal baroclinic waves were modified greatly. Under these circumstances, only a field of offshore eddies was left (§3) in the stress-free region, both upstream and downstream of the ridge. As a first step we measured the mean diameter of the offshore eddies, λ_0 (both cyclones and anticyclones). The values of λ_0/λ_s as a function of θ_* are shown in Fig. 6. Also shown in Fig. 6 for comparison are the plots of λ_w/λ_s (λ_w is the diameter of the waves measured at the upwelled front) taken from the experiments of NM1, since they also represent the size of the frontal waves of the present study when the upwelled front was far from the SDF. As can be seen, the size of the offshore eddies is almost twice the size of the waves at the upwelled front, i.e.,

$$\lambda_0 \approx 2\lambda_w, \tag{2}$$

and the eddies obey the same law as λ_w/λ_s versus θ_*, that is,

$$\frac{\lambda_w}{\lambda_s} \approx 0.15\theta_* \tag{3}$$

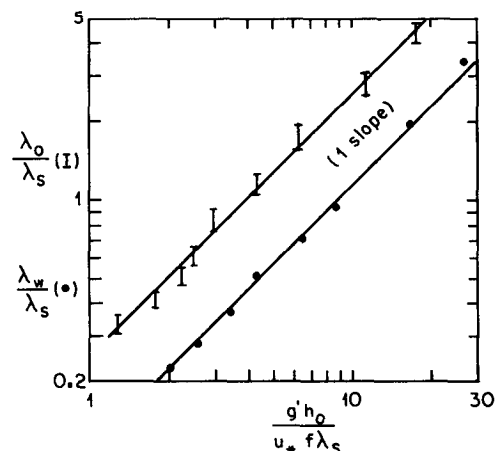$$\frac{\lambda_0}{\lambda_s} \approx 0.33\theta_*. \tag{4}$$

FIG. 6. The variation of λ_0/λ_s with θ_* (upper points), where λ_0 is the average diameter of the offshore eddies. The lower points are the variation of λ_w/λ_s with θ_*, taken from NM1, where λ_w is the average diameter of the frontal cyclones or anticyclones.

Relationships (3) and (4) can be rewritten as

$$\theta_w \approx \frac{g'h_0}{Uf\lambda_w} \approx 1, \tag{5}$$

$$\theta_0 = \frac{g'h_0}{Uf\lambda_0} \approx 2, \tag{6}$$

where $U \approx 10.6u_*$ (NM1) is the measured mean alongshore velocity of the top layer. We also measured the propagating speed (u_0) of these offshore eddies in the stress-free region, both upstream and downstream of the ridge, and to within an error of 10% to 15% our measurements were consistent with

$$\frac{u_0}{U} \approx 0.15. \tag{7}$$

Measurements of the maximum amplitude of the plume (see NM1), its migration, and its vacillation at the ridge when the front was far from SDF were the same as those already given in NM1. Later, when the plume maximum at the ridge interacted with SDF, the situation was different (see §3) and measurements of the aforementioned events became difficult because the flow field was so complicated.

The downstream jet flow of the present study was weaker than that of NM1 (see §3). We measured the distance D_{sw} of the first and largest of the standing waves downstream from the ridge (see Fig. 3). The values of D_{sw}/λ_s were then plotted as a function of θ_* and the results presented in Fig. 7. Also shown in Fig. 7 is a plot of the same quantities taken from the experiments of NM1. The values of D_{sw}/λ_s in the present experiments are 10% to 15% greater than those of NM1 and have the same dependence on θ_*. In NM1 we found

$$\theta_{sw} = \frac{g'h_0}{UfD_{sw}} \approx 0.5, \tag{8}$$

while for the present experiments we found

$$\theta_{sw} \approx 0.56. \tag{9}$$

5. Modes of offshore transport of upwelled fluid

In these experiments, for small values of θ_*, the upwelled front upstream of the ridge migrated far enough from the tank wall for the frontal baroclinic waves to interact fully with the SDF. We introduced dye at the wall to reveal the flow activities of the upwelled water near the surface, as described in section 2. The dyed, upwelled water drifted offshore in the Ekman flow until it reached the location of the frontal baroclinic waves at the SDF. Thereafter, the dyed, upwelled water was transported offshore by the flow generated by the interaction of the counterrotating offshore eddies. This is demonstrated in Fig. 8, where a number of these jets of upwelled, dyed water are shown. In Fig. 5 some of these offshore jets are revealed by particle streaks. Here, at locations where the particle streaks show offshore
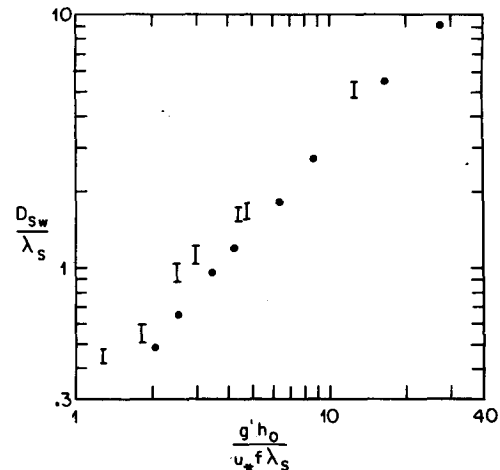

FIG. 7. The variation of D_{sw}/λ_s with θ_* (upper points), where D_{sw} is the distance of the first downstream standing wave from the ridge. The lower data are from NM1 and show a decrease of about 10% to 15% in magnitude from the results of the present experiment.

jets, the dyed, upwelled water is being transported offshore, indicating that these offshore jets, which are a result of the flow created by the counterrotating offshore eddies, represent one mechanism for transporting upwelled water offshore.

At higher values of θ_* the situation was different, since λ_s was smaller and the upwelled front did not interact strongly with SDF. Under these circumstances, a large offshore eddy usually formed in the stress-free region upstream of the ridge. Since this eddy was so large and so far offshore, it simply passed the ridge and interacted with the upwelling maxima there, causing a large quantity of the upwelled water to be transported offshore at the ridge (see Fig. 9). A similar situation was also observed in an experimental setup like that of NM1, as reported in Narimousa and Maxworthy (1986b). However, the large offshore eddy of Fig. 9 has also interacted with the downstream standing wave, resulting in counterrotating vortices and an offshore jet. As seen in Fig. 9, this jet has transported a considerable amount of the upwelled water offshore. Yet another example of offshore transport of the upwelled water by such an offshore eddy is shown in Fig. 10, where the value of θ_* is even greater than that of Fig. 9. In Fig. 10, the offshore eddy, after passing the ridge, interacted with the jet flow immediately downstream of the ridge and transported a large quantity of the upwelled water offshore.

Other possible mechanisms for producing offshore jets have been introduced in NM2 and NM1. In NM2, where SDF and the ridge were absent, at small values of θ_* the amplitude of the frontal instabilities was large and caused cyclones to pinch off from the front. These pinched-off cyclones propagated offshore in a similar way to the offshore eddies in the present study—i.e.,
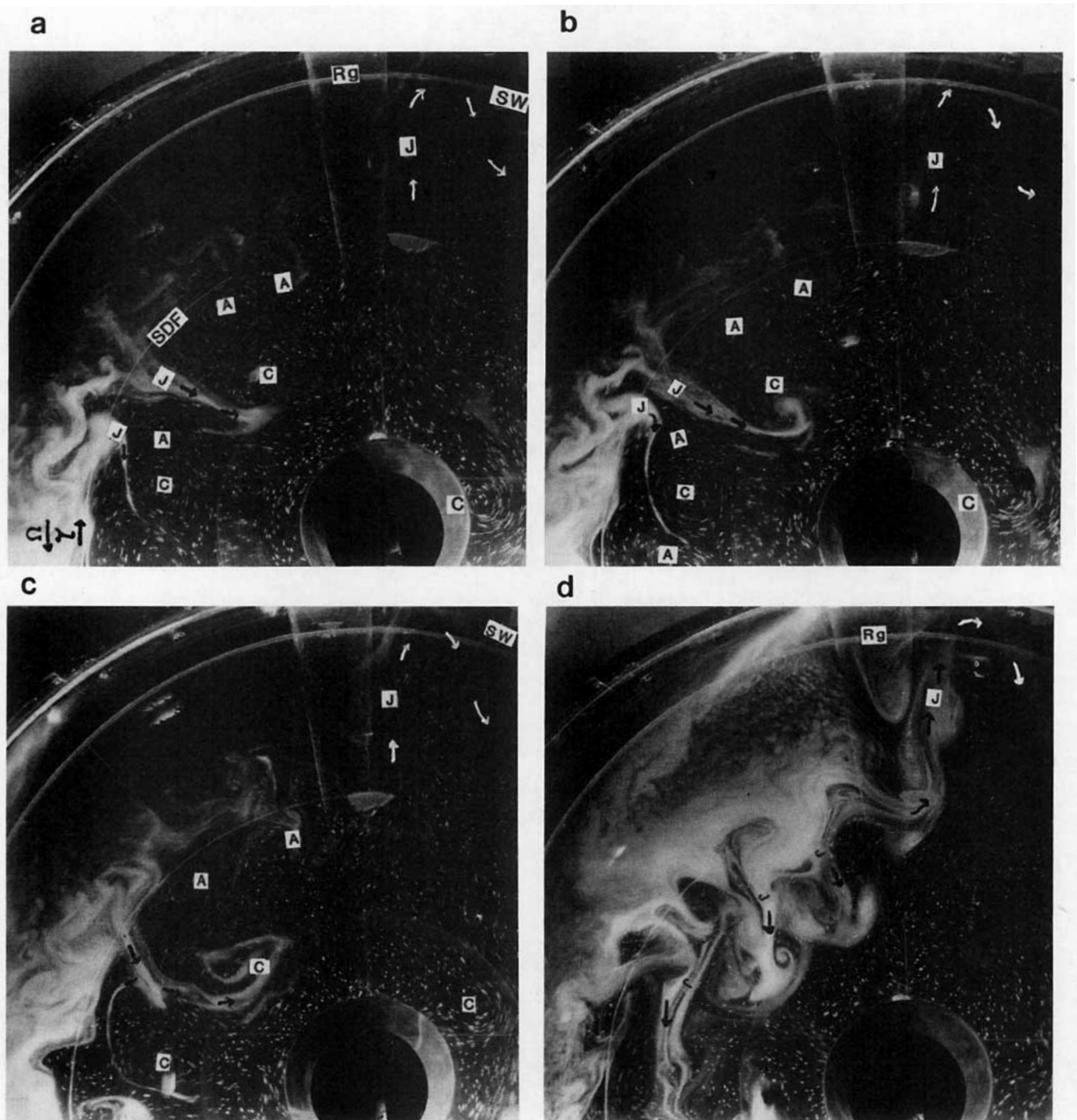
FIG. 8. A set of streak photographs, with a 0.5 s time exposure, from an experiment with $f = 4.65$ s^{-1}; $h_0 = 2$ cm; $g' = 22.5$ cm s^{-2}; $\Delta\Omega = 15.7$ s^{-1}; $u_* \approx 0.29$ cm s^{-1}; $\lambda_s = 18.4$ cm; $D \approx 20$ cm; and $\theta_* = 1.8$. In these photographs the direction of the turntable rotation Ω and the applied stress τ are indicated in (a). Also, offshore cyclones are indicated by (C) while anticyclones are indicated by (A). Photograph (a), taken after about $150T$, shows a number of offshore eddies and corresponding offshore jets (J), as shown by the particle streaks in the stress-free region upstream of the ridge. Notice that at the location of the offshore jets the dyed upwelled water is also transported off-shore. Photographs (b) and (c), taken 1 and $3T$ later than (a), respectively, show that upwelled water continues to be transported offshore. Photograph (d), taken $15T$ later than (a), shows that a large quantity of upwelled water has been transported offshore. In these photographs, like those of Fig. 5, the whole offshore eddy field is slowly drifting in the upstream direction. There is also a cyclonic offshore eddy downstream of the ridge that is propagating slowly toward the ridge. This eddy is far from the large amplitude wave at the ridge and the standing waves downstream of it, and it does not interact with them.
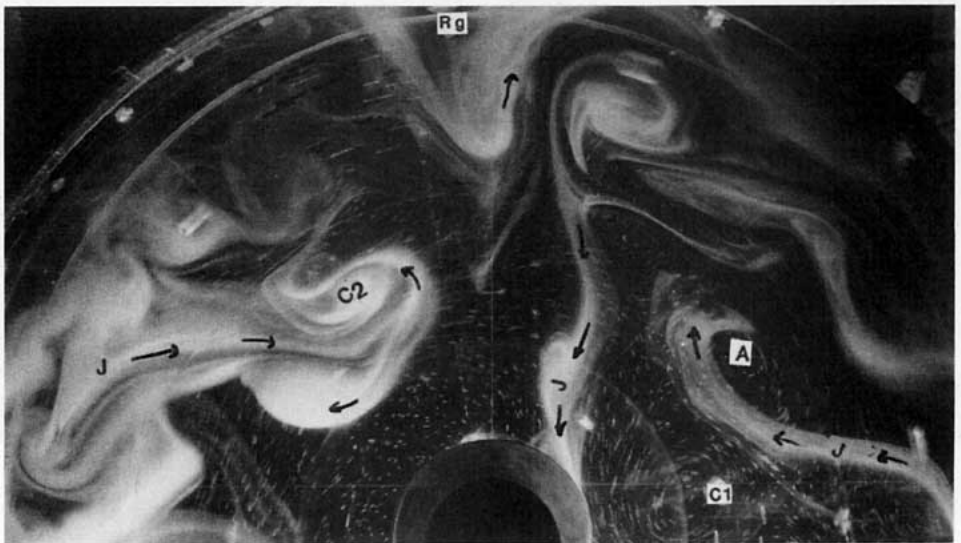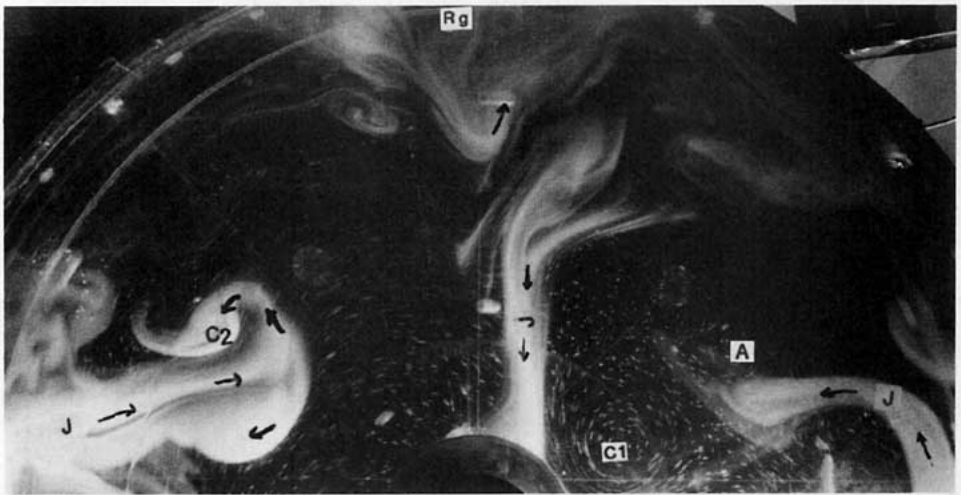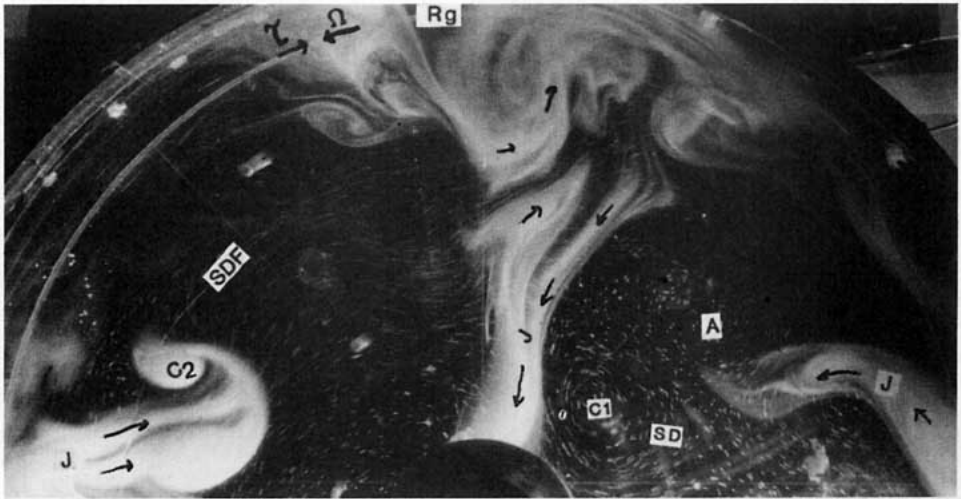
FIG. 9. A set of streak photographs, with a 0.5 s time exposure, from an experiment with $f = 2.7$ s^{-1}; $\Delta\Omega = 0.143$ s^{-1}; $h_0 = 2.4$ cm; $g' = 39$ cm s^{-2}; $u_* = 0.38$ cm s^{-1}; $\lambda_s \approx 7.5$ cm; $D = 17.6$; and $\theta_* \approx 12.3$. Photograph (a) (upper panel), taken after $190T$, shows an offshore cyclonic eddy (C_1), which has passed the ridge and has also interacted with the upwelling maximum at the ridge. As a result, a large quantity of upwelled water has been transported offshore all the way to the center of the tank. Photographs (b) (middle panel) and (c) (lower panel), taken 1 and $2T$ later than (a), respectively, show that the offshore cyclone
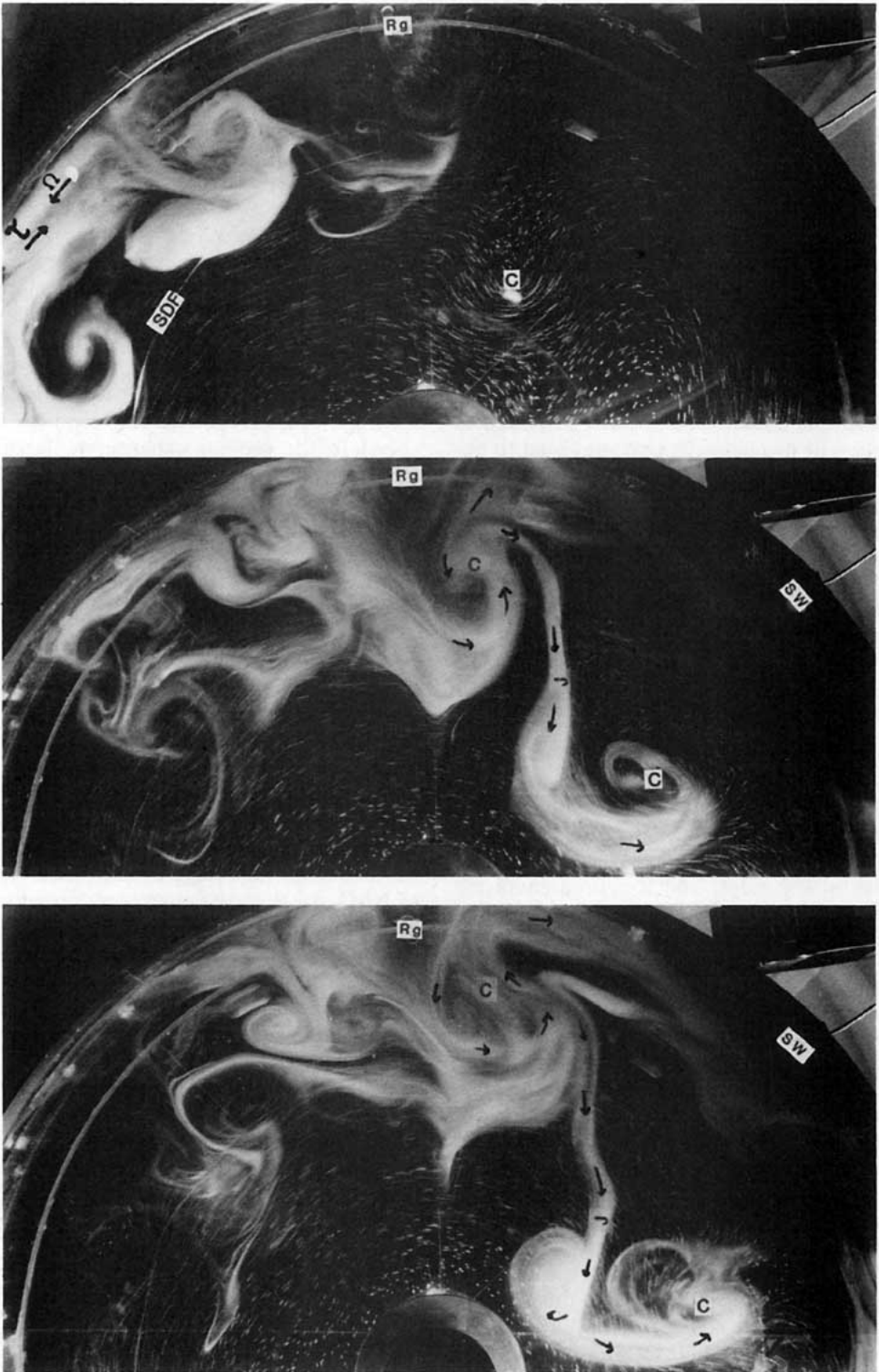
FIG. 10. A set of streak photographs, with a 0.5 s time exposure, from an experiment with $f = 2.8$ s^{-1}; $\Delta\Omega$ = 0.157 s^{-1}; $h_0 = 2.3$ cm; $g' = 51$ cm s^{-2}; $u_* = 0.42$ cm s^{-1}; $\lambda_s = 6.7$ cm; $D = 17.6$ cm; and $\theta_* = 14.85$. Photograph (a) (upper panel), taken after about $183T$, shows an offshore eddy that has just passed the ridge. Photographs (b) (middle panel) and (c) (lower panel), taken 7 and $9T$ later than (a), show that the offshore cyclone has interacted with the jet flow downstream of the ridge, and as a result, a large quantity of the upwelled water has been transported offshore.

propagates farther downstream and has interacted with the downstream standing waves to produce offshore jets there. In these photographs upstream of the ridge, an offshore eddy (C_2) has been generated at the SDF and propagated offshore, as in Fig. 2.

when these pinched cyclones interacted with frontal anticyclones, offshore jets were produced.

In NM1 the SDF was absent, but the presence of the ridge produced yet another mechanism from those discussed above. For small values of θ_* cyclonic eddies were observed to pinch off from the crest of the standing waves downstream of the ridge and to propagate offshore. This pinched-off cyclone then interacted with the downstream jet flow to produce offshore jets, which also transported the upwelled water offshore. Note that in the present experiments cyclonic eddies were not pinched off from the crest of the standing waves downstream of the ridge (see §3).

Thus, in summary, our models have suggested at least three different mechanisms that may lead to offshore jets: (a) instability of a standing wave downstream of a topographic ridge, as in NM1, which produced an offshore eddy; (b) large amplitude instabilities of the upwelled front itself, as in NM2, which also produced offshore eddies; and (c) production of offshore eddies due to the presence of an SDF, as in the present study. In all three cases the offshore eddies that were generated produced offshore jets.

6. Summary and conclusions

In the present experiments we have allowed a migrating, upwelling front to interact with a stress discontinuity front (SDF), beyond which the applied stress at the surface was zero. Interaction of the two fronts caused major changes in the appearance of the flow field upstream of the ridge, and it caused small but significant changes over and downstream of the ridge, when compared to experiments with a continuous stress distribution. These differences are as follows.

(i) At small values of θ_* a stationary, anticyclonic eddy, approximately two times the diameter of the frontal baroclinic waves (see NM1) developed at an early stage of the experiment in the stress-free region upstream and adjacent to the ridge. At a later time the rotation rate of this eddy became very large, the eddy began to drift upstream, and a cyclonic eddy replaced it. The size of this latter cyclone also increased to a value comparable to that of the original anticyclonic eddy. When it too became large, it began to drift upstream and was replaced by a growing anticyclonic eddy. This process was repeated several times. Since such upstream drift of the eddies was not observed in the experiments of NM1 and NM2, we may then suggest that the presence of the offshore curl in the present experiments is the most likely reason for the upstream drift of these eddies.

(ii) During development of the large stationary anticyclonic eddy adjacent to the ridge, successive large cyclones and anticyclones were observed upstream of the anticyclone in the stress-free region. These tended to drift very slowly in the upstream direction.

(iii) At larger values of θ_* large offshore eddies were observed to pass the ridge and interact with the upwelling maximum at the ridge or later with the downstream jet flow and standing waves to produce offshore jets transporting upwelled water offshore.

(iv) When the two fronts interacted strongly, the baroclinic frontal waves disappeared and lost all their energy to the larger eddies in the stress-free region, which at this stage were in direct contact with the upwelled front. These large eddies then transferred the upwelled fluid far offshore into the surrounding fluid in the form of jets.

(v) In those experiments in which the upwelled front interacted fully with SDF, the upwelling maximum at the ridge was weaker than that reported by NM1.

(vi) In the present experiment, large numbers of tracer particles accumulated at the intersection of the ridge with the SDF. This accumulation was not observed in the experiments of NM1. This observation might be important to the possible accumulation of marine life, oil slicks and perhaps waste material near bottom topography.

(vii) The general appearance of the jet flow downstream of the ridge was similar to that of NM1, although some detailed differences were apparent. For example, the jet of the present experiment was not as intense as that of NM1, and this caused the first downstream standing wave to occur farther from the ridge (10% to 15%) and to have a smaller amplitude (10% to 15%).

(viii) When the two fronts were not allowed to interact strongly, the flow field upstream, over and downstream of the ridge was virtually the same as that of NM1. In this case, weak, semipermanent, anticyclonic eddies, originally generated at the stress discontinuity front, were observed in the stress-free region. A similar type of eddy was also observed downstream of the ridge. Finally, the size of the upstream baroclinic waves increased considerably as the upwelling front approached the stress discontinuity.

(ix) The last and perhaps the most important result of the present study and those of NM1 and NM2 is that the offshore jets observed in these experiments were associated with offshore eddies generated in a variety of ways.

REFERENCES

Bernstein, R. L., L. C. Breaker and R. Whitmer, 1977: California current eddy formation: Ship, air and satellite results. *Science,* **195,** 353–359.

Breaker, C. L., and C. N. K. Mooers, 1985: Oceanic variability off the central California coast. Submitted to *Progress in Oceanography,* Pergamon.

Brink, K. H., D. Halpern and R. L. Smith, 1980: Circulation in the Peruvian upwelling system near 15°S. *J. Geophys. Res.,* **85,** 4036–4048.

Flament, P., L. Armi and L. Washburn, 1985: The evolving structure of an upwelling filament. *J. Geophys. Res.,* **90,** 11 783–11 798.

Griffiths, R. W., and P. F. Linden, 1981: The stability of buoyancy driven coastal currents. *Dyn. Atmos. Oceans,* **5,** 281–306.

Halpern, D., 1976: Structure of a coastal upwelling event observed off Oregon during July 1973. *Deep-Sea Res.,* **23,** 495–508.

——, 1977: Description of wind and of upper ocean currents and temperature variation on the Continental Shelf off Northwest Africa during March and April 1977. *J. Phys. Oceanogr.,* **7,** 722–430.

Hickey, B. M., 1979: The California Current System—hypothesis and facts. *Progress in Oceanography,* Vol. 8, Pergamon, 191–279.

Huyer, A., R. L. Smith and B. M. Hickey, 1984: Observation of a warm-core eddy off Oregon, January to March, 1978. *Deep-Sea Res.,* **31,** 97–117.

Ikeda, M., L. A. Mysak and W. J. Emery, 1984: Observation and modeling of satellite-sensed meanders and eddies off Vancouver Island. *J. Phys. Oceanogr.,* **14,** 3–21.

Linden, P. F., and F. J. F. Van Heijst, 1984: Two-layer spin-up and frontogenesis. *J. Fluid Mech.,* **143,** 69–94.

Maxworthy, T., 1977: Topographic effects in rapidly-rotating fluids: Flow over a transverse ridge. *Z. Angew. Math Phys.,* **28,** 853–864.

Mooers, C. N. K., and A. R. Robinson, 1984: Turbulent jets and eddies in the California current and inferred cross-shore transports. *Science,* **223,** 52–53.

——, C. A. Collins and R. S. Smith, 1976: The dynamics structure of the frontal zone in the coastal upwelling region off Oregon. *J. Phys. Oceanogr.* **6,** 3–21.

Narimousa, S., and T. Maxworthy, 1985: Two-layer model of shear driven coastal upwelling in the presence of bottom topography. *J. Fluid Mech.,* **159,** 503–531.

——, and ——, 1986a: Coastal upwelling on a sloping bottom; the formation of plumes, jets and pinched-off cyclones. *J. Fluid Mech.* (in press).

——, and ——, 1986b: Laboratory modeling of coastal upwelling. *Eos, Trans. Amer. Geophys. Union,* **67,** 2–3.

Nelson, C. S., 1977: Wind stress and wind stress curl over the California current. NOAA Tech. Rep. NMFS SSRF-714, U.S. Dept. of Commerce, 89 pp.

Rienecker, M. M., C. N. K. Mooers, D. E. Hagan and A. R. Robinson, 1985: A cool anomaly off Northern California: An investigation using IR imagery and in situ data. *J. Geophys. Res.,* **190,** 4807–4818.

Saunders, P. M., 1973: The instability of a baroclinic vortex. *J. Phys. Oceanogr.,* **3,** 61–65.

Simpson, J. J., T. D. Dickey and C. J. Koblinsky, 1984: An offshore eddy in the California current system. *Progress in Oceanography,* Vol. 13, Pergamon, 5–49.